PAPER • OPEN ACCESS

The benefit of Ca in improving pinning of $BaZrO_3$ - Y_2O_3 doubly-doped $YBa_2Cu_3O_{7-}$, $/Ca_{0.3}Y_{0.7}Ba_2Cu_3O_{7-x}$ multilayer nanocomposite films

To cite this article: Mohan Panth et al 2023 Mater. Res. Express 10 046001

View the article online for updates and enhancements.

You may also like

- High critical current density over 1 MA cm² at 13 T in BaZrO₉ incorporated Ba(Fe,Co)₂As₂ thin film Jongmin Lee, Jianyi Jiang, Fumitake Kametani et al.
- New insight into strain and composition of BaZrO₃ nanorods in REBCO superconductor Goran Majkic, Jong Seok Jeong, Hwanhui Yun et al.
- Enabling coherent BaZrO₃
 nanorods/YBa₂Cu₂O_{7x} interface through dynamic lattice enlargement in vertical epitaxy of BaZrO₃/YBa₂Cu₃O_{7x}
 nanocomposites
 Judy Z Wu, Victor Ogunjimi, Mary Ann

Materials Research Express



OPEN ACCESS

RECEIVED

20 December 2022

REVISED

9 March 2023

ACCEPTED FOR PUBLICATION

27 March 2023

PUBLISHED

4 April 2023

Original content from this work may be used under the terms of the Creative Commons Attribution 4.0 licence

Any further distribution of this work must maintain attribution to the author(s) and the title of the work, journal citation and DOI.



PAPER

The benefit of Ca in improving pinning of BaZrO₃- Y_2O_3 doubly-doped YBa₂Cu₃O_{7-x}/Ca_{0.3}Y_{0.7}Ba₂Cu₃O_{7-x} multilayer nanocomposite films

Mohan Panth^{1,*}, Victor Ogunjimi¹, Mary Ann Sebastian^{2,3}, Bibek Gautam¹, Timothy Haugan² and Judy Wu^{1,*}

- 1 Department of Physics and Astronomy, the University of Kansas, Lawrence, KS 66045, United States of America
- ² U.S Air Force Research Laboratory, Aerospace Systems Directorate, WPAFB, OH 45433, United States of America
- ³ University of Dayton Research Institute, Dayton, OH 45469, United States of America
- * Authors to whom any correspondence should be addressed.

E-mail: panthm@ku.edu and jwu@ku.edu

Keywords: artificial pinning centers, BZO/YBCO interface, multilayer, lattice mismatch, vortex pinning

Abstract

This work examines the pinning enhancement in BaZrO₃ (BZO) +Y₂O₃ doubly-doped (DD) YBa₂Cu₃O₇ (YBCO) nanocomposite multilayer (DD-ML) films. The film consists of two 10 nm thin Ca_{0.3}Y_{0.7}Ba₂Cu₃O_{7-x} (CaY-123) spacers stacking alternatively with three BZO + Y₂O₃/YBCO layers of 50 nm each in thickness that contain 3 vol% of Y₂O₃ and BZO doping in the range of 2–6 vol%. Enhanced magnetic vortex pinning and improved pinning isotropy with respect to the orientation of magnetic field (B) have been achieved in the DD-ML samples at lower BZO doping as compared to that in the single-layer counterparts (DD-SL) without the CaY-123 spacers. For example, the pinning force density (F_p) of ~58 GNm⁻³ in 2 vol.% of DD-ML film is ~110% higher than in 2 vol% of DD-SL at 65 K and B//c-axis, which is attributed to the improved pinning efficiency by c-axis aligned BZO nanorods through diffusion of Calcium (Ca) along the tensile-strained channels at BZO nanorods/YBCO interface for improvement of the interface microstructure and hence pinning efficiency of BZO nanorods. An additional benefit is in the considerably improved $J_c(\theta)$ and reduced J_c anisotropy in the former over the entire range of the B orientations. However, at higher BZO doping, the BZO nanorods become segmented and misoriented, which may change the Ca diffusion pathways and reduce the benefit of Ca in improving the pinning efficiency of BZO nanorods.

1. Introduction

The c-axis-aligned one-dimensional artificial pinning centers (1D-APCs), such as nanorods of BaZrO₃ (BZO), BaSnO₃ (BSO), BaHfO₃ (BHO), and YBa₂(Nb/Ta)O₆, in high temperature superconducting (HTS) REBaCu₃O_{7-x} (RE = Y, Gd, Sm) films provide strong correlated pinning at B//c-axis [1–10]. However, the strain field originated from the lattice mismatch at the 1D-APC/REBCO interface could result in reduced superconducting transition temperature (T_c) and critical current density (J_c) at temperatures close to T_c [11–14]. Doping of APCs with mixed morphologies of 1D (nanorods), 2D (nanoplates), and 3D (nanoparticles or NPs) has been explored to reduce the modulated strain field associated to the high-concentration 1D-APC arrays [6, 15–19]. Reduced T_c degradation and anisotropy of J_c and pinning force density (F_p) to the orientation of the applied magnetic field are among the benefits of doping of APCs with mixed morphologies. Among others, double doping (DD) of 1D-APCs and 3D-APCs of Y_2O_3 NPs, such as BZO + Y_2O_3 , BHO + Y_2O_3 , and BSO + Y_2O_3 in YBCO has been extensively studied [15, 20, 21]. High and Isotropic J_c is demanded for high-temperature superconducting applications because it ensures that the superconductor has the same critical current density in all directions including motors, generators, transformers, magnetics, etc [22–25]. Jha et al reported reduced I_c anisotropy from 180% to 80% with 3 areal% of Y₂O₃ and 3 vol.% BSO concentrations in YBCO as compared to its singly-doped (SD) counterpart (with BSO only) at 65 K and 1 T [15]. Similarly, Chen et al observed reduced anisotropy in BZO + Y_2O_3 DD films of varying BZO concentrations of 2–6 vol.% and 3 vol.% of Y_2O_3 [4]. J_c

anisotropy as low as 18% has been observed at 65 K and 9 T by Gautam *et al* in YBCO DD films containing 2 vol. % of BHO +3 vol.% of Y_2O_3 [21].

We recently reported a multilayer (ML) approach to improve the BZO 1D-APC pinning efficiency by diffusing Calcium (Ca) from thin $Ca_{0.3}Y_{0.7}Ba_2Cu_3O_{7-x}$ (CaY-123) spacers to BZO/YBCO layers stacked alternatively with the spacers [26, 27]. The observed pinning enhancement is attributed to modification of the BZO 1D-APC/YBCO interface. Specifically, the diffusion of Ca into YBCO at the interface is argued to be driven by the tensile strain on YBCO lattice, resulting in formation of short segments of stacking faults in the YBCO columns near the interface associated to the Ca/Cu substitution on the Cu-O plane of YBCO and hence elongation of the c-axis constant of YBCO for reduced lattice mismatch at the BZO 1D-APC/YBCO interface [27].

In this work, we explore the combination of the DD and ML approaches by carrying out a comparative study of BZO + Y_2O_3 DD films made in the ML (DD-ML) and single-layer (DD-SL) configurations, seeking further enhancement of pinning. Specifically, the study aims to explore whether the improved BZO pinning efficiency by Ca diffusion could be implemented in DD-ML samples for both enhanced J_c and reduced anisotropy. Both DD-ML and DD-SL samples have a fixed 3 vol.% of Y_2O_3 doping (with -4% lattice mismatch with YBCO), while the BZO (with +7.7% lattice mismatch with YBCO) concentration was varied to 2, 4 and 6 vol.%, while previous studies have only examined the ML approach in BZO-doped YBCO films without Y_2O_3 [27–31]. Many studies have been conducted on DD-SL YBCO films with the goal of enhancing J_c and angular isotropic J_c through the use of mixed APCs [4, 6, 15, 20, 21, 32, 33]. These investigations have focused on improving the pinning properties of the films, which is crucial for maximizing the performance of high-temperature superconductors. Our previous research found that the ML approach improves pinning by repairing defective interfaces through Ca/Cu replacement, resulting in a 5-fold increase in pinning force density in ML films compared to SL films. In this study, we systematically examine the DD-ML approach for the first time to determine if the ML approach still improves pinning in these films compared to DD-SL films. In the following, we report the experimental result.

2. Experimental

Two ML film sets containing single doping (SD) and double-doping (DD) of BZO concentrations of 2, 4, and 6 vol.%, respectively were fabricated using pulsed laser deposition (PLD) from BZO doped YBCO targets of the nominal compositions. PLD targets contain 3 vol.% of Y₂O₃ for the fabrication of DD samples. In order to make DD-ML samples, a CaY-123 PLD target was adopted for deposition of the two CaY-123 spacer layers of thickness ~10 nm each deposited alternatively with three BZO + Y₂O₃/YBCO layers. Therefore, the YBCO DD-ML films have a multilayer structure with three \sim 50 nm thick BZO + $Y_2O_3/YBCO$ layers separated by two alternating 10 nm thin CaY-123 spacers. The films were deposited on (100) SrTiO₃ (STO) single crystal substrates. A KrF excimer laser (wavelength \sim 248 nm, pulse energy \sim 450 mJ) was used to ablate the target material. The distance between the target and the substrate is set to 5.5 cm. The PLD repetition rates of 8 Hz and 2 Hz is used for the BZO + Y₂O₃/YBCO and CaY-123 layers. The deposition temperature was 825 $^{\circ}$ C and the oxygen partial pressure of 300 mTorr has been maintained. The samples are referred to as 2% DD-ML, 4% DD-ML, and 6% DD-ML respectively for ease of reference. A set of reference samples of 2% DD-SL, 4% DD-SL, and 6% DD-SL, were fabricated for comparison with DD-ML samples. DD-SL samples were fabricated using PLD conditions similar to that for DD-ML samples except for the missing CaY-123 spacers. All PLD fabricated samples were annealed in situ at 500 °C in one atmospheric oxygen pressure for 30 min after the deposition. It should be noted that the PLD conditions for $BZO + Y_2O_3/YBCO$ layers was optimized based on the previous studies [8, 17, 34]. Tencor P-16 profilometer was used to measure the film thicknesses. The DD-SL and DD-ML films typically have thicknesses of 150–170 nm each. The transmission electron microscopy (TEM) were used for cross-sectional images of the samples by using a Thermo Fisher Scientific Themis-Z TEM system which is an aberration-corrected electron microscope with a spatial resolution as small as 63 pm at an acceleration voltage of 300 kV with combined correctors. Crystallinity and lattice parameters were determined by x-ray diffraction (XRD) utilizing a Bruker D8 Discover diffractometer. In DD samples, c-axis aligned BZO one dimensionalartificial pinning centers (BZO 1D-APCs) of diameter ~5–6 nm were confirmed at low BZO concentration of 2 vol.% [28, 35], which are replaced with segmented BZO 1D-APCs with a large splay angle range at high BZO concentrations.

Electric transport properties were measured on two parallel microbridges fabricated on each film using photolithography. Wet etching with 0.05% nitrous acid was adopted to remove the unwanted nanocomosite films around the two microbridges. The finished microbridges have lengths of 500 μ m and widths of 20 and 40 μ m, respectively. The details of the photolithography process can be found in our prior works [17, 35]. Silver (Ag) contact pads of ~1 mm in diameter and ~120 nm in thickness were deposited through a shadow mask on all

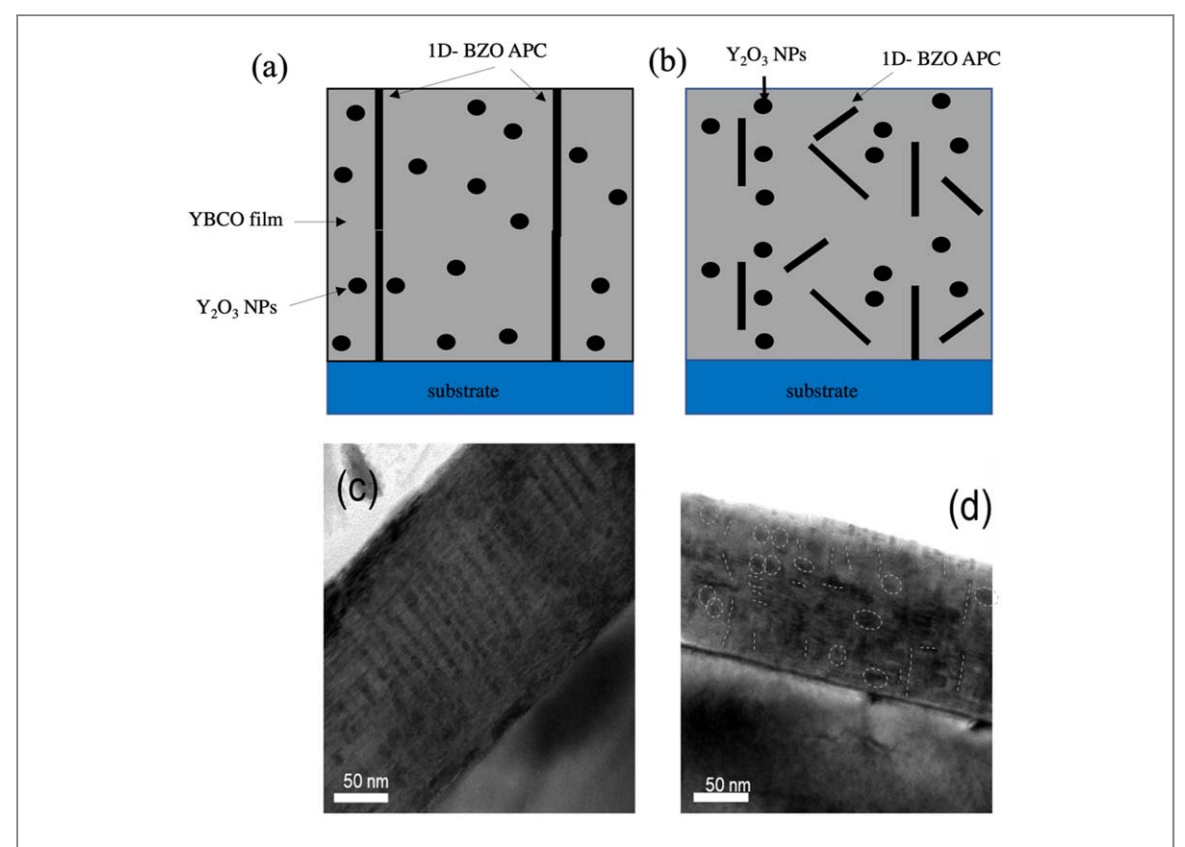


Figure 1. Schematic description of microstructures of the YBCO DD-SL films at (a) lower BZO doping (2%-4%) and (b) higher BZO doping. Cross-sectional TEM images are exhibited on a (c) 4% DD-SL and (d) 6% DD-SL samples respectively.

samples using DC magnetron sputtering before photolithography to ensure good electric contacts. The deposition rate for Ag was ~0.07 nm/second under an argon pressure of 30 mTorr,. The electric power used for the Ag sputtering is around 34 watts. Platinium wires of 50 μ m were attached to the Ag pads using Indium to make the electrical connection to the microbridges. Critical current density (J_c) was measured at different applied magnetic fields B in the range of 0–9 T at temperatures of 65–77 K in a Quantum Design Ever-Cool II Physical Property Measurement System (PPMS). The transport properties (T_c and J_c) were measured using the standard four-probe technique. The J_c measurement was taken at different B field orientations ranging from θ = 0° (B//c-axis) to θ = 90° (B//ab-plane) in the plane with B perpendicular to J_c . The J_c (B) values were calculated using a standard voltage criterion of 1 μ V/cm. The pinning force density (F_p) was calculated using the equation $F_p = J_c \times B$. The maximum pinning force density ($F_{p,max}$) and its corresponding magnetic field (B_{max}) were determined from the F_p (B) curves.

3. Results and discussion

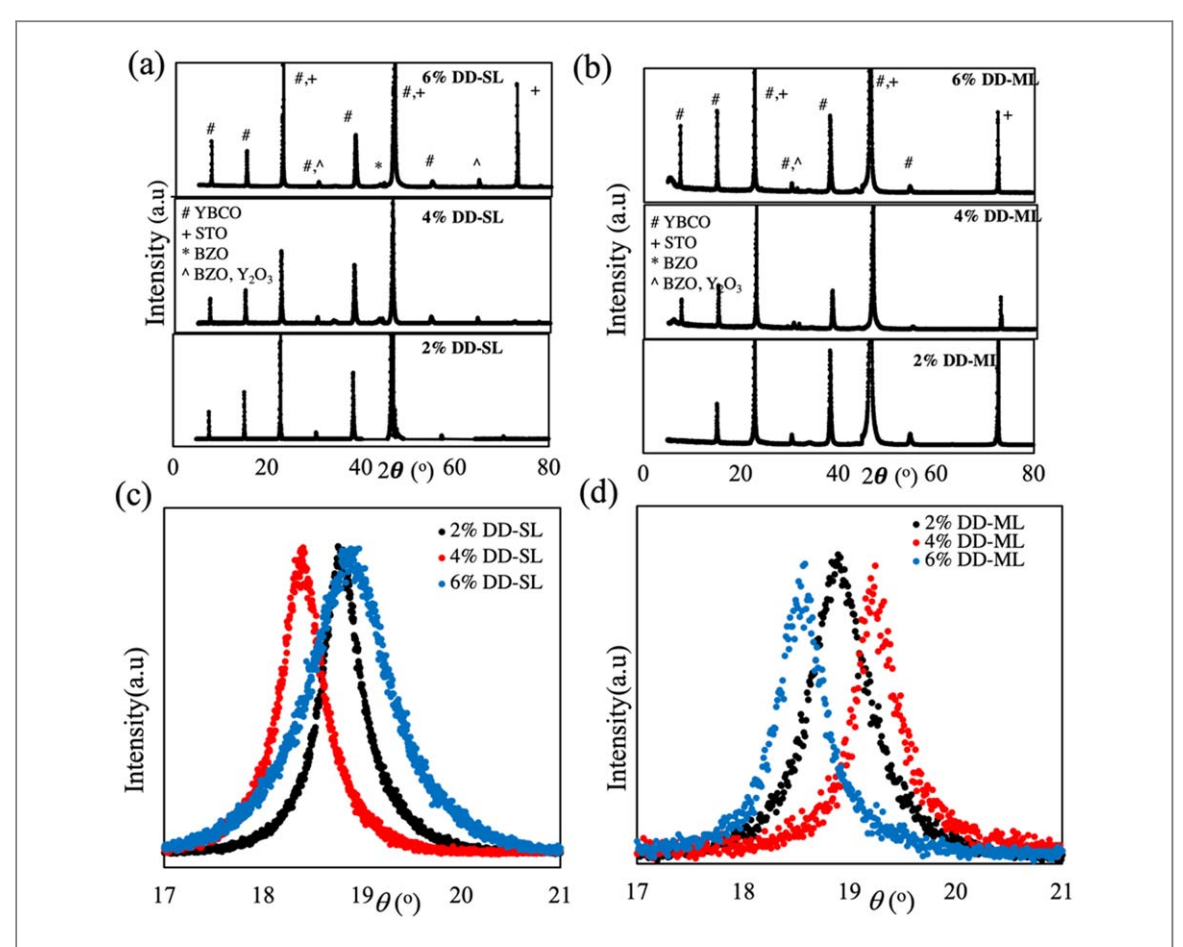


Figure 2. XRD θ –2 θ spectra taken on (a) 2, 4, and 6% YBCO DD-SL and (b) 2, 4, and 6% YBCO DD-ML films. YBCO (005) rocking curves taken on (c) 2, 4, and 6% YBCO DD-SL films and (d) 2, 4, and 6% YBCO DD-ML films. The spectra were generated using Cu-k α radiation of wavelength 1.54 Å. The symbols #, +, *, and ^ represent the YBCO (001), STO substrate (100), BZO (001), and BZO/Y₂O₃ peaks respectively.

level increases. In the 6% SD-SL sample, the midpoint between BZO 1D-APCs is approximately around 3 nm, where the strain field reaches around 80% of its maximum value. Incorporating Y_2O_3 3D-APCs is likely to induce local alteration in the strain field, and this effect would be more pronounced at higher BZO doping levels. As a result, the self-assembly of APCs in the DD-SL samples may be altered. This leads to the formation of short segments of BZO 1D-APCs with a broad range of the splay angles deviating from the c-axis of the YBCO film. This configuration is shown schematically in figure 1(b) and is confirmed by the experimental TEM image in figure 1(d). This leads to a significantly reduced concentration of the c-axis-aligned BZO 1D-APCs (dashed lines in figure 1(d)).

It is worth noting that in this work, a $BaZrO_3 + Y_2O_3/YBCO$ layer of 50 nm in thickness was grown as the first layer in both DD-SL and DD-ML samples. This means the microstructures shown in figure 1 are indicative of both DD-SL and DD-ML samples since the CaY-123 spacers are not expected to alter the morphology, orientation, and concentration of the APCs. This argument has been confirmed in the reported SD-ML nanocomposite films [26, 27, 30, 37], which suggests that a modulated strain field may be maintained in the DD-ML samples with low BZO doping but not necessarily at a higher level of BZO doping.

The XRD θ – 2θ spectra of 2%, 4%, and 6% YBCO DD-SL and ML films are compared in figures 2(a) and (b) respectively. The appearance of the (001) YBCO peaks indicates YBCO nanocomposite films with c-axis orientation on a (100) STO substrate. The Y₂O₃ peak at ~32° confirms the presence of Y₂O₃ NPs in the DD films. In addition, a major BZO (001) peak can be seen at ~40° in all samples as expected. The low peak intensity of BZO and Y₂O₃ peaks in figures 2(a) and (b) indicates that the doping concentration in the DD-SL and DD-ML nanocomposite films is low. Estimation of the YBCO c-lattice constants is based on the YBCO (005) peaks. The c-lattice constants of the DD-SL films are 11.75 Å, 11.72 Å, and 11.74 Å respectively for 2%, 4%, and 6% YBCO DD-SL films (see table 1). Comparable c-lattice constants of 11.72 Å, 11.73 Å, and 11.76 Å are observed respectively for 2%, 4%, and 6% YBCO DD-ML films. Compared with the c-lattice constant of 11.67 Å for undoped YBCO [38], the BZO doped YBCO samples have considerably larger c-axis lattice constants which are indicative of tensile strain along the c-axis in doped YBCO films [12, 13, 39] and the reduced lattice mismatch

Sample ID	APC doping (vol.%)	$T_{c}(K)$	FWHM (005) YBCO (°)	c lattice parameter (Å)	$F_{p,max}(77K)GN/m^3$	$F_{p, max}(65 \text{ K}) \text{ GN/m}^3$
2% DD-SL	$2 \text{ vol.} \% \text{ BZO} + 3\% \text{ Y}_2\text{O}_3$	85.7	0.486	11.75	0.71	52.48
2% DD-ML	$2 \text{ vol.} \% \text{ BZO} + 3\% \text{ Y}_2\text{O}_{3+} \text{ CaY-spacer layer}$	84.0	0.638	11.72	2.14	57.46
4% DD-SL	$4 \text{ vol.} \% \text{ BZO} + 3\% \text{ Y}_2\text{O}_3$	87.6	0.471	11.72	3.33	49.49
4% DD-ML	$4 \text{ vol.} \% \text{ BZO} + 3\% \text{ Y}_2\text{O}_{3+} \text{CaY-spacer layer}$	84.0	0.446	11.73	1.71	34.81
6% DD-SL	$6 \text{ vol.} \% \text{ BZO} + 3\% \text{ Y}_2\text{O}_3$	87.8	0.957	11.74	3.95	67.5
6% DD-ML	6 vol.% BZO $+$ 3% Y $_2\mathrm{O}_3$ $_+$ CaY-spacer layer	85.5	0.483	11.76	2.10	28.47

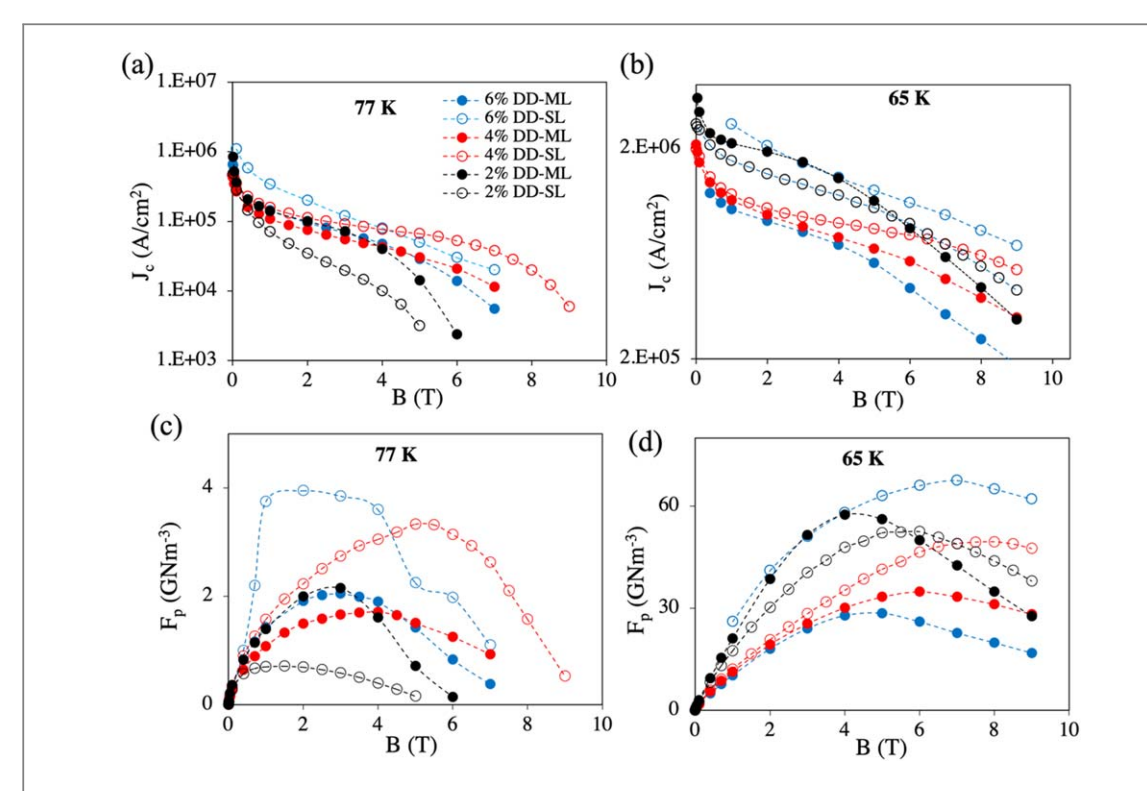


Figure 3. A comparison of $J_c(B)$ curves taken on (a) 2, 4, and 6% DD-SL (open) and DD-ML (solid) samples at (a) 77 K (b) 65 K, respectively. The J_c measurements were carried out at B/C. A comparison of $F_p(B)$ plots for 2, 4, and 6% DD-SL (open) and DD-ML (solid) samples at (c) 77 K (d) 65 K respectively.

between BZO and YBCO near the BZO/YBCO interface by Ca substitution occurs locally as observed in BZO/YBCO SD-ML samples [26, 27, 40].

The crystallinity of the DD-SL and DD-ML films was further analyzed in (005) YBCO rocking curves shown in figure 2(c) (DD-SL films) and 2d (DD-ML films) respectively where black, red, and blue curves represent 2%, 4%, and 6% films. The full-width-at-half-maximum (FWHM) values of the (005) peak are 0.486°, 0.471°, and 0.957° for 2%, 4%, and 6% YBCO DD-SL films. The values are 0.638°, 0.446°, and 0.483° for 2%, 4%, and 6% YBCO DD-ML films respectively. These FWHM values (table 1) do not show any trend with changing BZO concentration for both sets of the DD-SL and DD-ML films, which is similar to the previous report for other DD-SL (BSO + Y_2O_3) YBCO nanocomposite films by Jha *et al* [15]. Nevertheless, the relatively small FWHM values observed suggest the crystallinity is preserved in the DD-SL and DD-ML films.

The T_c values were determined from the R-T curves measured on the DD-SL and DD-ML films and the values are summarized in table 1. Specifically, the T_c values for 2, 4, 6% DD-SL films are 85.7 K, 87.6 K, and 87.8 K which are slightly higher than the 84.0 K, 84.0 K, and 85.5 K for their DD-ML counterparts. The reduced T_c values in the ML samples may be attributed to the overdoping effect of Ca on the YBCO [26, 27, 41, 42]. In addition, the monotonic increase of the T_c values with increasing BZO doping concentration in the case of DD-SL as well as DD-ML films is consistent with previous reports as the consequence of strain relief through defect formation [8, 15].

Figures 3(a) and (b) compare the $J_c(B)$ curves of the 2%–6% DD-SL (open) and DD-ML (solid) films at B//c in the field range of 0–9 T at a temperature of 77 K and 65 K respectively. Opposite trends of $J_c(B)$ have been observed in the comparison at lower (2%) and higher (4%–6%) BZO doping. respectively. In the former, the DD-ML film outperforms its DD-SL counterpart with a higher J_c value over the entire magnetic field range at 77 K as seen in figure 3(a). For example, the J_c enhancement factors of 1.9, 3.6, and 4.5 times can be observed on the 2% DD-ML film at 1 T, 3 T, and 5 T respectively over that of the 2% DD-SL film. In contrast, the 4% and 6% DD-ML films have lower $J_c(B)$ values as compared to their DD-SL counterparts'. Higher J_c values are observed mostly for the entire field range with increasing BZO doping concentration in the case of DD-SL films. However, lower J_c is observed in DD-ML films with increasing BZO doping contrary to DD-SL films. At 65 K, in figure 3(b), similar behavior is seen in the comparison of the DD-SL and DD-ML films except for a crossover in the $J_c(B)$ curves at around ~5T for the 2% DD-SL and DD-ML films. Figures 3(c) and (d) compare the $F_P(B)$ curves measured on DD-SL and DD-ML samples at B//c-axis and at 77 K and 65 K respectively. All curves have a similar inverted bell shape with the maximum pinning force density $F_{p,max}$ at the peak position of B_{max} (table 1). The enhanced $J_c(B)$ leads to an enhanced $F_p(B)$ for the 2% DD-ML films at both 77 K and 65 K over most B field

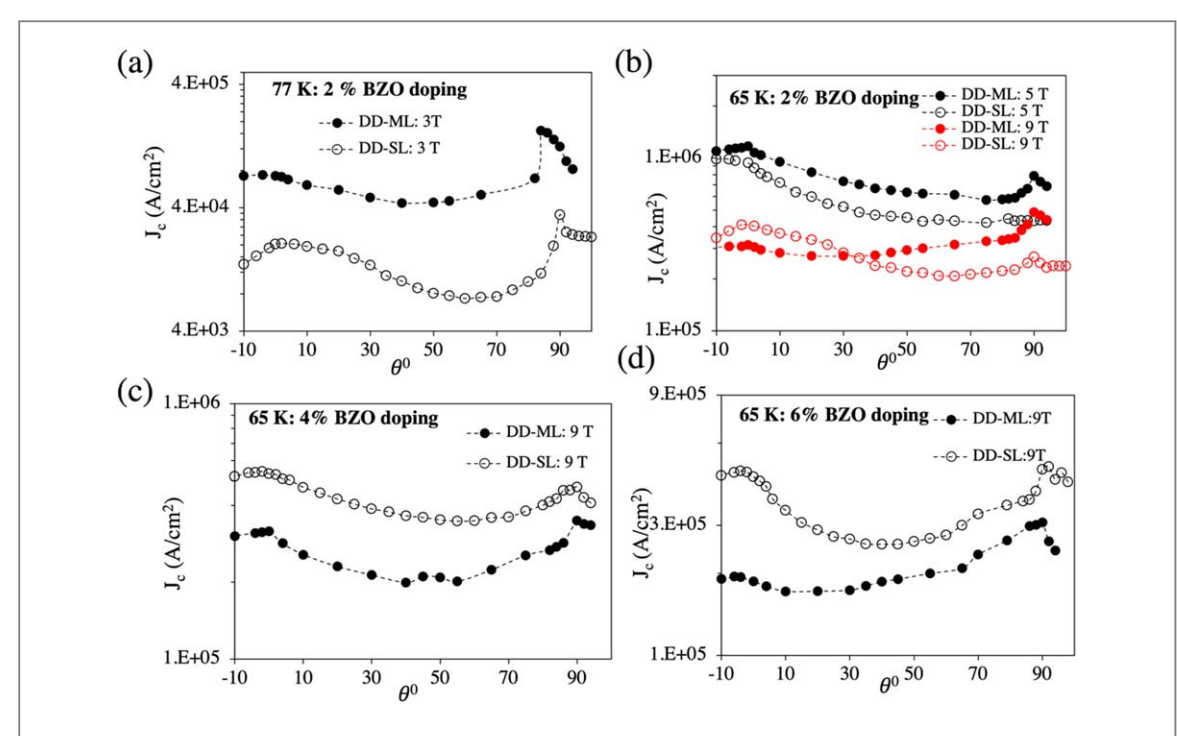


Figure 4. A comparison of $J_c(\theta)$ curves of 2% DD-SL and DD-ML samples at (a) 77 K and 3 T, and (b) 65 K and 5 T and 9 T, respectively. A comparison of $J_c(\theta)$ curves of (c) 4% DD-ML and DD-SL films at 9 T and 65 K, and (d) 6% DD-ML and DD-SL films at 9T and 65 K, respectively.

range. For example, the $F_{p,max}$ of 2.14 GNm⁻³ is almost 4 times higher than that of the 2% DD-SL at 77 K. In contrast, the $F_p(B)$ for 4% and 6% DD-ML samples are lower than their DD-SL counterparts'. Therefore, the benefit of Ca diffusion is limited to low BZO concentration of 2% in the DD-ML samples, which is in contrast to the enhanced pinning for 2%–8% BZO/YBCO.

SD-ML samples as compared to their SD-SL counterparts [40]. This observation supports our argument that it is the well-modulated tensile strain at the BZO 1D-APC/YBCO interface that provide the diffusion channel for Ca ions from the CaY-123 spacers and facilitate the Ca/Cu substation on the Cu-O planes of YBCO near the interface since the replacement of smaller Cu by a larger Ca ion (by ~30%) is energetically preferred in the tensile strained interface. In DD-SL and DD-ML samples, the modulated strain field associated to the c-axis-aligned BZO 1D-APCs is disturbed by the doping of Y_2O_3 3D-APCs. This disturbance increases with BZO doping as evidenced in the decreasing concentration of the through-thickness, c-axis-aligned BZO 1D-APCs at higher BZO concentration. Even at the lowest BZO doping of 2%, this disturbance may still reduce the Ca diffusion along the BZO 1D-APC/YBCO interface quantitatively and limit the benefit of Ca to low fields.

Figures 4(a) and (b) compare the $J_c(\theta)$ curves of 2% DD-ML and 2% DD-SL at 77 K and 65 K respectively at a few selected B fields. The 2% DD-ML shows higher J_c values than the 2% DD-SL in the entire angular range at 77 K and 3 T (figure 4(a)). Specifically, an enhancement factor of five is observed. At 65 K, a prominent J_c peak at B//c-axis is observed for both films at 5 T (black) and 9 T (red) as shown in figure 4(b), which is attributed to the correlated pinning arising from the c-axis aligned BZO 1D-APCs. The J_c anisotropy, defined as $(J_{c,max}-J_{c,min})/J_{c,min}$, is ~128% and ~88% respectively for the DD-SL and DD-ML films at 5 T. At 9 T, reduced anisotropy of ~97% and ~72% for the DD-SL and DD-ML films are observed. This result indicates the benefit of Ca includes enhanced $J_c(B)$ and reduced anisotropy in $J_c(\theta)$ in the 2% DD-ML samples. In contrast, the $J_c(\theta)$ curves of 4% and 6% DD-ML films show lower $J_c(\theta)$ values as compared to their DD-SL counterparts due to lack of efficient Ca diffusion channels along the tensile strained BZO 1D-APC/YBCO interface. However, it is unclear why DD-ML samples with 4 and 6% BZO doping have reduced the $J_c(B)$ and the $J_c(\theta)$. While Ca doping of YBCO may lead to considerable T_c decrease, the damage on APC pinning properties is not anticipated and demands further research.

Figure 5 compares four different types of nanocomposites samples, namely SD-ML, SD-SL, DD-ML, and DD-SL, of 2% and 6% BZO doping at 65 K. In both 2% and 6% cases, the SD-ML films (red) have the highest $J_c(B)$ values as shown in figures 5(a) and (b). This suggests the coherent BZO 1D-APC/YBCO interface plays a critical role in determining the pinning efficiency of BZO 1D-APCs as the dominant pinning centers in both SD and DD cases. Figures 5(c) and (d) compare $F_p(B)$ of the same films as in figures 5(a) and (b). Again, the SD-ML samples at both 2% and 6% doping show the overall highest $F_p(B)$. In these two samples, the $F_{p,max}$ are 97.3 GNm⁻³ and 157.7 GNm⁻³ are observed. Interestingly, at lower field <5T, the 2% DD samples outperform the 2%

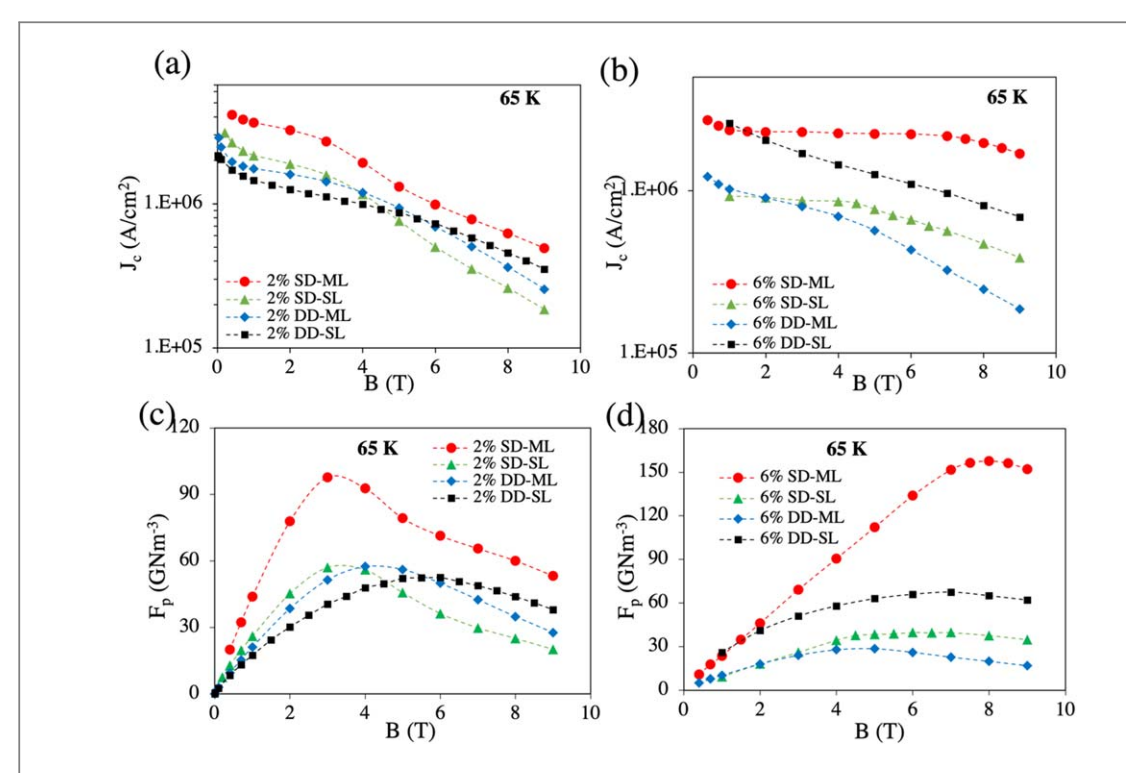


Figure 5. A comparison of $J_c(B)$ curves taken on the SD-ML, SD-SL, DD-ML, and DD-SL samples with (a) 2% and (b) 6% BZO doping in BZO/YBCO nanocomposites. A comparison of the $F_p(B)$ curves of the same SD-ML, SD-SL, DD-ML, and DD-SL samples with (c) 2% and (d) 6% BZO doping respectively. B//c-axis in all cases.

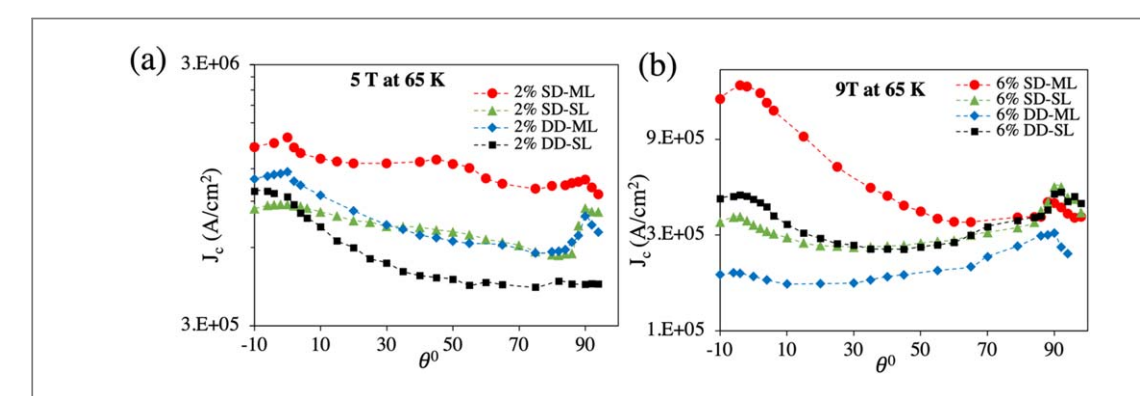


Figure 6. (a) A comparison of $I_c(\theta)$ curves taken on SD-ML, SD-SL, DD-ML, and DD-SL nanocomposite films with (a) 2% BZO doping at a magnetic field of 5 T, and (b) 6% BZO doping at a magnetic field of 9 BZO doping at T.

SD-SL sample while the 6% DD samples have lower $F_p(B)$ in the entire B field range. Considering the $F_p(B)$ was measured at B//c-axis, this is not surprising since the c-axis aligned BZO 1D-APCs are reduced in DD samples.

The $J_c(\theta)$ curves measured at 65 K are compared in figures 6(a) and (b) for 2% and 6% films at a magnetic field of 5T and 9T respectively. Intriguingly, the SD-ML films (red) at both BZO doping levels have the highest J_c values almost for the entire angular range of $\theta=0^\circ$ (B//c-axis) to $\theta=90^\circ$ (B//c-ab-plane). Specifically, the J_c enhancement at B//c-axis is 1.7 times for 2% SD-ML samples as compared to SD-SL counterparts at 5T and 65 K and it is 4.7 times for 6% SD-ML samples as compared to the 6% SD-SL samples at 9 T and 65 K. This result indicates strong pins, such as c-axis aligned BZO 1D-APCs with improved pinning efficiency using the ML scheme could provide enhanced pinning even at B orientations away from the c-axis. Furthermore, the two 2% DD samples (green and blue) also exhibit higher $J_c(\theta)$ than the 2% SD-SL (black) sample's at 5T (figure 6(a)) while the trend is reversed at 9 T (figure 6(b)), indicating that the mixed APCs in the DD samples are favorable for high and isotopic pinning at moderate B fields while the through thickness BZO 1D-APCs are stronger pins at higher B fields.

Figures 7(a) and (b) compare the microstructure of the SD-SL and SD-ML BZO/YBCO nanocomposite films. In the former, a tensile-strain YBCO column (in green color) of a few nm in thickness forms around the

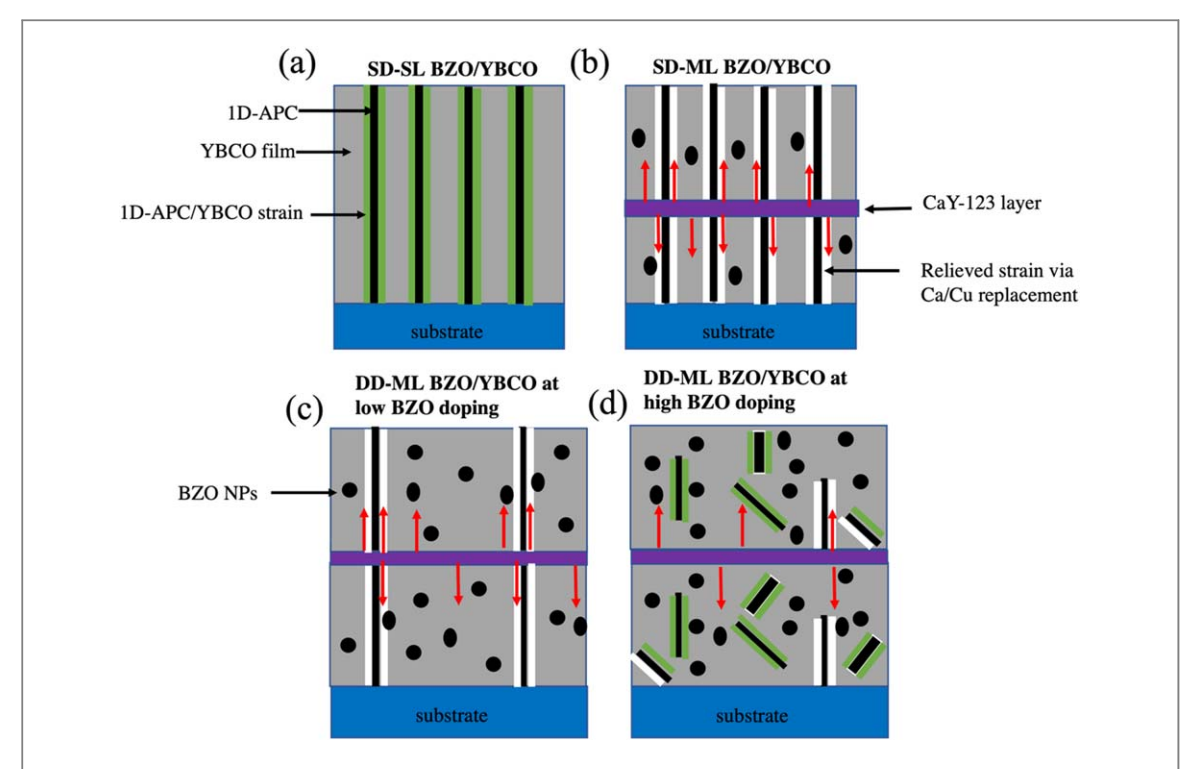


Figure 7. Hypothetical schematics of microstructures of (a) SD-SL, (b) SD-ML BZO/YBCO nanocomposite films. The green column around the c-axis aligned BZO 1D-APC highlights the tensile strained YBCO column around the BZO 1D-APC due to the large BZO/YBCO lattice mismatch of ~7.7%. The red arrows in (b) depict the Ca-diffusion from the CaY-123 spacers along the tensile strained BZO/YBCO interface. The consequent elongation of the YBCPO c-axis leads to a reduced BZO/YBCO lattice mismatch to ~1.4% and reduces the tensile strain in the YBCO column (white). The similar strain-driven Ca diffusion may be preserved in DD-ML samples at low BZO doping (~2%) (c) but may be inefficient at higher BZO doping (d).

BZO 1D-APC due to the large BZO/YBCO lattice mismatch of ~7.7% [11, 12]. This column provides a Ca diffusion channel (indicated by red arrows along the column) in the SD-ML sample (figure 7(b)). Ca ion is ~30% larger than Cu ion [43] and the Ca/Cu substitution on the Cu-O plane of YBCO has been found energetically favorable in tensile-strained YBCO column, resulting in YBCO c-axis elongation and reduced BZO/YBCO lattice mismatch to ~1.4% [26, 27, 31]. Consequently, the tensile strain in the YBCO column is much reduced (shown in white) and the BZO/YBCO interface is almost defect-free or coherent. The overall highest $J_c(B)$ and $J_c(\theta)$ in SD-ML samples as compared to others studied in this work suggest the importance of the BZO/YBCO interface on pinning efficiency. When the ML scheme is applied to the DD samples, the tensile-strain directed Ca diffusion along the BZO/YBCO interface may be maintained at low BZO doping (figure 7(c)), which explains the improved pinning in 2% DD-ML sample and no pinning enhancement in DD-ML films with higher BZO doping since the modulated strain field is altered by the Y_2O_3 NPs and the Ca diffusion channel is no longer present (figure 7(d)). This means the benefit of Ca diffusion relies on the presence of a Ca diffusion channel along the tensile-strained YBCO column at the BZO/YBCO interface. It should be noted that Ca diffusion into BZO/YBCO layers may occur via other channels, while no positive effect on pinning has been observed.

The enhancement of the magnetic vortex pinning in the ML-SD and ML-DD (at low BZO doping of 2%) samples led to overall improvement in the properties of the samples. The increase in pinning force density and J_c allowed for the superconductor to carry more current without resistance, which is essential for many applications such as motors, generators, and transformers. The reduction of anisotropy in J_c also improved the uniformity of current flow and reduced the risk of hot spots, which can cause damage to the device. Our study showed that the ML approach can be used to in SD and DD doping cases to enhance pinning and improve the overall properties of the samples, resulting in improved J_c and reduced anisotropy [26–28, 30, 40]. While in the SD case, a similar modulated strain field is present as the BZO doping is varied from 2% to 8% [30], it is disturbed in the DD case. Further modification of the ML approach is necessary to maintain the modulated strain to facilitate the Ca diffusion along the BZO 1D-APC/YBCO interface for enhanced pinning efficiency of the 1D-APCs. This will make an interesting research topic in future research for improvement of pinning in superconductors for various applications.

4. Conclusions

In summary, this study evaluates the combined effects of double-doping and multilayer approaches on the pinning of the DD-ML nanocomposite films with fixed 3 vol.% Y₂O₃ concentration and variable BZO concentrations of 2, 4, and 6 vol.%, respectively. Several important observations have been made in this study. First, it has been found that the benefits of the two approaches can be combined to yield higher and less anisotropic I_c if the Ca diffusion from CaY-123 spacers to the BZO/YBCO nanocomposite layer could be controlled through the tensile-strained YBCO columns formed around the BZO 1D-APCs to prevent the formation of a defective BZO/YBCO interface, which enhance the pinning efficiency of the BZO 1D-APCs. This explains the observed enhancement of pinning in 2% DD-ML sample as compared to that of its counterpart DD-SL sample. Quantitatively, the $F_{\rm pmax}$ of ~58 GNm⁻³ at 65 K and B//c-axis observed in the former is more than twice of that in the latter. Furthermore, the enhanced pinning efficiency of the BZO 1D-APCs also lead to enhanced $J_c(\theta)$ over the entire θ range or B field orientation, indicative of an extended benefit of the Ca-induced improved pinning strength in BZO 1D-APCs. This leads to reduced I_c anisotropy with respect to the B field orientations in the 2% DD-ML sample. Finally, when the modulated tensile strained YBCO column is disturbed in DD samples with higher BZO doping, the benefit of Ca diffusion becomes negligible or even negative, suggesting the pinning enhancement via other pathways of Ca diffusion into APC/YBCO nanocomposite films is unlikely. Importantly, the comparison of the SD-SL, SD-ML, DD-SL, and DD-ML samples has revealed that the BZO 1D-APCs with a coherent interface with YBCO play a dominant role in pinning of these nanocomposite films as illustrated in the overall highest $J_c(B)$ and $J_c(\theta)$ in the SD-ML samples.

Acknowledgments

This research was supported in part by NSF contracts Nos: NSF-DMR-1508494 and 1909292 and NSF-ECCS-1809293, the AFRL Aerospace Systems Directorate, the Air Force Office of Scientific Research (AFOSR) LRIR #14RQO8COR and LRIR #18RQCOR100.

Data availability statement

All data that support the findings of this study are included within the article (and any supplementary files).

ORCID iDs

References

- [1] MacManus-Driscoll J et al 2004 Strongly enhanced current densities in superconducting coated conductors of YBa 2 Cu 3 O 7-x + BaZrO 3 Nat. Mater. 3 439-43
- [2] Wu J and Shi J 2017 Interactive modeling-synthesis-characterization approach towards controllable *in situ* self-assembly of artificial pinning centers in RE-123 films *Supercond. Sci. Technol.* 30 103002
- [3] Miura S et al 2017 Strongly enhanced irreversibility field and flux pinning force density in SmBa2Cu3O y-coated conductors with well-aligned BaHfO3 nanorods Appl. Phys. Express 10 103101
- [4] Chen S et al 2017 Generating mixed morphology BaZrO3 artificial pinning centers for strong and isotropic pinning in BaZrO3–Y2O3 double-doped YBCO thin films Supercond. Sci. Technol. 30 125011
- [5] Mele P et al 2008 Ultra-high flux pinning properties of BaMO3-doped YBa2Cu3O7—x thin films (M = Zr, Sn) Supercond. Sci. Technol. 21 032002
- [6] Gautam B et al 2017 Transformational dynamics of BZO and BHO nanorods imposed by Y2O3 nanoparticles for improved isotropic pinning in YBa2Cu3 O 7- δ thin films AIP Adv. 7 075308
- [7] Gautam B et al 2018 Probing the effect of interface on vortex pinning efficiency of one-dimensional BaZrO3 and BaHfO3 artificial pinning centers in YBa2Cu3O7-x thin films Appl. Phys. Lett. 113 212602
- [8] Chen S et al 2017 Enhancement of isotropic pinning force in YBCO films with BaZrO3 nanorods and Y2O3 nanoparticles IEEE Trans. Appl. Supercond. 27 4–8
- [9] Galstyan E et al 2021 Pinning Characteristics of Zr and Hf-Added REBCO Coated Conductors Made by Advanced MOCVD in Low-to-High Magnetic Fields IEEE Trans. Appl. Supercond. 31 1–5

- [10] Matsumoto K and Mele P 2009 Artificial pinning center technology to enhance vortex pinning in YBCO coated conductors Supercond. Sci. Technol. 23 014001
- [11] Cantoni C et al 2011 Strain-driven oxygen deficiency in self-assembled, nanostructured, composite oxide films ACS Nano 5 4783-9
- [12] Horide T et al 2017 Structural evolution induced by interfacial lattice mismatch in self-organized YBa2Cu3O7 δ NANOCOMPOSITE Film ACS Nano 11 1780–8
- [13] Horide T et al 2014 Elastic strain evolution in nanocomposite structure of YBa2Cu3O7 + BaZrO3 superconducting films Jpn. J. Appl. Phys. 53 083101
- [14] Wee S H et al 2013 Self-assembly of nanostructured, complex, multication films via spontaneous phase separation and strain-driven ordering Adv. Funct. Mater. 23 1912–8
- [15] Jha A K et al 2015 Tailoring the vortex pinning strength of YBCO thin films by systematic incorporation of hybrid artificial pinning centers Supercond. Sci. Technol. 28 114004
- [16] Sebastian M A et al 2019 Comparison study of the flux pinning enhancement of YBa 2 Cu 3 O 7 δ thin films with BaHfO 3 + Y 2 O 3 single-and mixed-phase additions IEEE Trans. Appl. Supercond. 29 1–5
- [17] Sebastian M A P et al 2017 Study of the flux pinning landscape of ybco thin films with single and mixed phase additions BaMO3 + Z: M = Hf, Sn, Zr and Z = Y2O3, Y211 IEEE Trans. Appl. Supercond. 27 1–5
- [18] Ding F et al 2012 Enhanced flux pinning in MOD-YBCO films with co-doping of BaZrO3 and Y2O3 nanoparticles J. Alloys Compd. 513 p. 277–81
- [19] Feldmann D et al 2010 1000 A cm 1 in a 2 μ m thick YBa2Cu3O7 x film with BaZrO3 and Y2O3 additions Supercond. Sci. Technol. 23 115016
- [20] Horide T et al 2013 Jc improvement by double artificial pinning centers of BaSnO3 nanorods and Y2O3 nanoparticles in YBa2Cu3O7 coated conductors Supercond. Sci. Technol. 26 075019
- [21] Gautam B et al 2018 Microscopic adaptation of BaHfO3 and Y2O3 artificial pinning centers for strong and isotropic pinning landscape in YBa2Cu3O7-x thin films Supercond. Sci. Technol. 31 025008
- [22] Gamble B B et al 2002 The status of HTS motors in IEEE Power Engineering Society Summer Meeting (IEEE)
- [23] Hull JR and Strasik M 2013 Concepts for using trapped-flux HTS in motors and generators Physica C 484 p 104-7
- [24] Gao Y et al 2019 Design and study of a 2G HTS synchronous motor with brushless HTS flux pump exciters IEEE Trans. Appl. Supercond. 29 1–5
- [25] Shaanika E et al 2019 Core loss of a bulk HTS synchronous machine at 2 and 3 T rotor magnetisation IEEE Trans. Appl. Supercond. 30
- [26] Ogunjimi V et al 2021 Enhancing magnetic pinning by BaZrO3 nanorods forming coherent interface by strain-directed Ca-doping in YBa2Cu3O7—x nanocomposite films Supercond. Sci. Technol. 34 104002
- [27] Wu J Z et al 2022 Enabling coherent BaZrO3 nanorods/YBa2Cu3O7-x interface through dynamic lattice enlargement in vertical epitaxy of BaZrO3/YBa2Cu3O7-x nanocomposites Supercond. Sci. Technol. 35 034001
- [28] Baca F J et al 2013 Interactive Growth Effects of Rare-Earth Nanoparticles on Nanorod Formation in YBa2Cu3Ox Thin Films Adv. Funct. Mater. 23 4826–31
- [29] Ogunjimi V et al 2021 Enhancing Magnetic Pinning by BaZrO3 Nanorods Forming Coherent Interface by Strain-Directed Ca-doping in YBa2Cu3O7-x Nanocomposite Films Supercond. Sci. Technol. 34 104002
- [30] Panth M et al 2022 Multilayer YBa 2 Cu 3 O 7-x/Ca 0.3 Y 0.7 Ba 2 Cu 3 O 7-x nanocomposite films with 2-8% BaZrO 3 doping for high-field applications IEEE Trans. Appl. Supercond. 32 8001208
- [31] Panth M et al 2022 Multilayer YBa 2 Cu 3 O 7-x/Ca 0.3 Y 0.7 Ba 2 Cu 3 O 7-x Nanocomposite Films With 2–8% BaZrO 3 Doping for High-Field Applications *IEEE Trans. Appl. Supercond.* 32 1–8
- [32] Jha A K et al 2017 Isotropic enhancement in the critical current density of YBCO thin films incorporating nanoscale Y2BaCuO5 inclusions J. Appl. Phys. 122 093905
- [33] Jha A K et al 2016 Controlling the critical current anisotropy of YBCO superconducting films by incorporating hybrid artificial pinning centers IEEE Trans. Appl. Supercond. 26 1–4
- [34] Wang X et al 2010 Eliminating thickness dependence of critical current density in YBa 2 Cu 3 O 7 x films with aligned BaZrO 3 nanorods J. Appl. Phys. 108 113911
- [35] Wu J et al 2015 Controlling BaZrO3 nanostructure orientation in YBa2Cu3O films for a three-dimensional pinning landscape Supercond. Sci. Technol. 28 125009
- [36] Shi JJ and Wu JZ 2011 Transition of impurity nanorod orientation in epitaxial ybco films on vicinal substrates ArXiv Preprint arXiv 1112 5612
- [37] Kiessling A et al 2011 Nanocolumns in YBa2Cu3O7 x/BaZrO3 quasi-multilayers: formation and influence on superconducting properties Supercond. Sci. Technol. 24 055018
- [38] Liang R et al 1992 Growth and properties of superconducting YBCO single crystals Physica C 195 51–8
- $[39] Cava\ R\ et\ al\ 1990\ Structural\ anomalies, oxygen\ ordering\ and\ superconductivity\ in\ oxygen\ deficient\ Ba2YCu3Ox\ Physica\ C\ 165\ 419-33$
- [40] Panth M et al 2022 Temperature dependent pinning efficiency in multilayer and single layer BZO/YBCO nanocomposite films. in IOP Conf. Ser.: Mater. Sci. Eng. (IOP Publishing)
- [41] Hammerl G et al 2000 Enhanced supercurrent density in polycrystalline YBa2Cu3O7-δ at 77 K from calcium doping of grain boundaries Nature 407 162–4
- [42] Daniels GA, Gurevich A and Larbalestier DC 2000 Improved strong magnetic field performance of low angle grain boundaries of calcium and oxygen overdoped YBa 2 Cu 3 O x Appl. Phys. Lett. 77 3251–3
- [43] Klie R et al 2005 Enhanced current transport at grain boundaries in high-T c superconductors Nature 435 475–8